

Retina Phantom Model for Hyperspectral Imaging

Michelle D. Bryarly^{a,b}, Minh Ha Tran^{a,b}, Arrsh Ali,^{a,b} Baowei Fei^{a, b, c*}

^a Department of Bioengineering, University of Texas at Dallas, Richardson, TX;

^b Center for Imaging and Surgical Innovation, University of Texas at Dallas, Richardson, TX

^c Department of Radiology, University of Texas Southwestern Medical Center, Dallas, TX;

* Corresponding author: bfei@utdallas.edu, Website: <https://fei-lab.org>

ABSTRACT

Accurate retinal imaging is crucial for preclinical research and the development of diagnostic and therapeutic approaches for eye diseases. However, existing retinal imaging models often lack the precision needed to replicate the complex optical environment of the eye, limiting their effectiveness in testing and calibration. Current approaches rely heavily on live animals, which pose ethical concerns and variability in results. In this work, we designed a retinal phantom that can be used to validate spatial and spectral properties. We developed a 3D-printed mouse phantom retina to simulate the conditions of the eye and mimic its optical qualities. We produced gelatin phantom with deoxygenated blood to simulate veins and arteries. Imaging was performed using a topical endoscopic fundus imaging (TEFI) hyperspectral camera. For data analysis, we estimated the oxygenation rate in the phantom. The results showed that the phantom had rich both spatial and spectral details. Oxygenation mapping shows that the phantom produced reliable oxygenation rates of the blood. We believed that this work can be used by researchers for the purpose of validating HSI cameras and may be iterated upon to simulate eye diseases.

Keywords: hyperspectral imaging, phantom model, retina imaging, eye diseases, topical endoscopic fundus imaging.

1. INTRODUCTION

Hyperspectral Imaging (HSI) is an imaging modality that captures images at multiple wavelengths. Because of the unique spectral information of different tissues, HSI can be used to identify, extract, and analyze biomarkers and monitor diseases [1]. Within the last 20 years, engineering progress has produced hyperspectral cameras that are more compact, have better performances, and cheaper compared to their predecessors [2]. As such, they found increasingly more uses in various fields, including biological and medical fields. Hyperspectral imaging can be potentially used for the screening of Alzheimer's disease [3], detecting tumors for surgical resection [4], and predicting instances of macular degeneration [5]. Using hyperspectral imaging to estimate and map oxygen saturation remains one of the more common usages [6-11]. We can further divide oxygenation mapping into two types: mapping the tissue oxygenation rate, and mapping blood oxygenation rates within vessels. For examples of the first type, Chin *et al.* [6] used tissue oxygenation to predict severity of burns; Schmidt *et al.* [7] used oxygenation mapping to identify healing of tissues after treatments; and Sakota *et al.* [8] used oxygenation mapping to evaluate quality of anastomosis. For examples of the second type, Mordant *et al.* [9] identified that patients with glaucoma have higher venular saturation compared to healthy controls; Akbari *et al.* [10] used vessels mapping to detect arteries and veins during surgery; and Aref *et al.* [11] used vessels mapping to aid phlebotomy.

Even though HSI does not have the depth of optical coherent tomography (OCT), it can extract retinal biomarkers that OCT cannot [12]. With advances in more compact and faster systems, HSI has seen more uses in the monitoring and diagnosis of many other retinal diseases. Beyond what is visually seen through fundus imaging (drusen, cotton wool spots, *etc.*), the power of HSI came from quantifying changes in the spectral profiles of biological features. HSI can quantify the oxygenation rate of blood vessels in the retina [13-15]. HSI can also identify high deposits of chemicals in the retina such as amyloid-beta proteins [3, 16]. For example, Harvey *et al.* [13] performed preliminary studies on mapping oxygenation rate around the optic nerve head for people with diabetic retinopathy. Li *et al.* [14] used HSI on histological retina slice to determine the effectiveness of diabetic retinopathy treatments. Yao *et al.* [17] used machine learning to classify stages of diabetic retinopathy by looking at both spatial and spectral features. Rose *et al.* [15] identify changes in retinal perfusion in patients with radiation retinopathy by means of oxygen mapping.

There are significant challenges in retinal HSI research. One such problem is the lack of proper models of study. There are many logistical hurdles when it comes to procuring biological tissues. Hyperspectral phantoms are cost-effective to manufacture, do not spoil over time, and approximate their biological counterparts. A good hyperspectral phantom approximates not only the biological features of the real-life tissue, but also the spectral features. Blood is a dominant chromophore and is often the main simulated tissue [18-22]. Phantoms with blood aim to simulate the oxygenation properties and spectra of hemoglobin. Blood can be oxygenated mechanically by exposure to pure oxygen or to inert gases like nitrogen [18]. It can also be deoxygenated chemically by sodium dithionite [19-22] ($\text{Na}_2\text{S}_2\text{O}_4$, also known as sodium hydrosulfite). For anatomical accuracies, 3D printing techniques can be used. Ghassemi *et al.* [23] built a biological phantom of the retina equipped with blood vessels. The model has some deviation from the original image, but they were able to achieve channels of diameters less than 1 mm. While the Ghassemi model proved useful for studying humans, there is a lack of attention toward making and studying of animal phantoms. Since researchers mainly work on animal models before moving to clinical studies, animal retina phantoms should be a direction of research for the future.

In this paper, we improved upon previous retinal designs to build small animal retina phantoms. The phantoms were designed for HSI systems, so both spatial and spectral contents were considered. We modelled the optical characteristic of the mouse eyes and the reflective characteristic of the blood vessels. We used a modified topical fundus endoscopic imaging (TEFI) [24] to capture high-resolution images of the phantom, thereby validating it. We showed some preliminary results on a larger blood phantom, manufactured using gelatin and glass tube with diameter around 1 mm. Our study was the first step toward standardizing small animal retinal phantoms for hyperspectral imaging in the future.

2. METHODS

Lens Holder Design

Figure 1 shows the list of phantoms for different mammals. Human retina phantom came from a commercial phantom (OEM-7, Ocular Instruments, USA). The phantom has a pupil diameter of 7 mm. The retina structure consisted of blood vessels, optic disc, and simulated foreign body. Rat retina phantom used the same dimensions as that of Hosseinaee *et al* [25]. The phantom has an iris diameter of 6 mm and focal length of 6 mm. Mouse phantom included several improvements upon Hosseinaee's design. As mouse and rat eyes differ in size by linear factor of 1.9-2.0, our mouse phantom opening models an interior diameter of 3.1 mm (~0.12 in) with an opening of 2.7 mm (~0.11 in) [26].

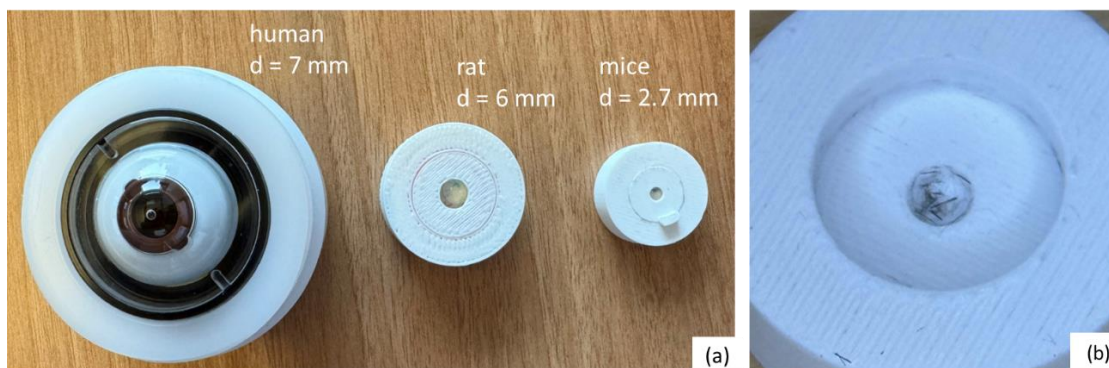


Figure 1. (a) List of phantoms for the retina. From left to right: Human phantom (pupil diameter ~7 mm), rat phantom (pupil diameter ~6 mm), mouse phantom (pupil diameter ~2.7 mm). (b) Opened mouse retina phantom, showing carbon fibers with diameter 5 μm to simulate small blood vessels.

Figure 2 shows the 3D model of the mouse eye phantom. The lens holder was created to model the lens size, axial length, and focal length of a mouse eye. We adapted a previous design [25] to suit the anatomical characteristics of a mouse. Our lens holder accommodates a mouse lens model with a diameter of 4 mm (~0.16 in) and a height of 2.3 mm (~0.09 in), effectively simulating the natural curvature of a mouse lens [26]. The lens is made of borosilicate glass material, with a refractive index of 1.5168 [27]. Similarly, healthy adult C57BL6 mice lenses were found experimentally by C. Cheng *et al.* to have a maximum refractive index of ~1.55 [28]. Another key aspect considered during the design process was the

smaller vitreous-to-lens ratio in mouse eyes compared to human eyes. In mice, the lens occupies 65-75% of the eye [29, 30]. To replicate this proportion, the anterior chamber phantom features a depth (focal length) of 1.5 mm (~0.059 in). The design process was carried out using Creo Parametric computer-aided design (CAD) software. The final design uses generic PLA white filament as its material, which has an average assumed rate of shrinkage range of 0.8% to 3%. The model was 3D printed using a Bambu Labs X1 Carbon printer with a 0.4 mm (about 0.02 in) nozzle print head.

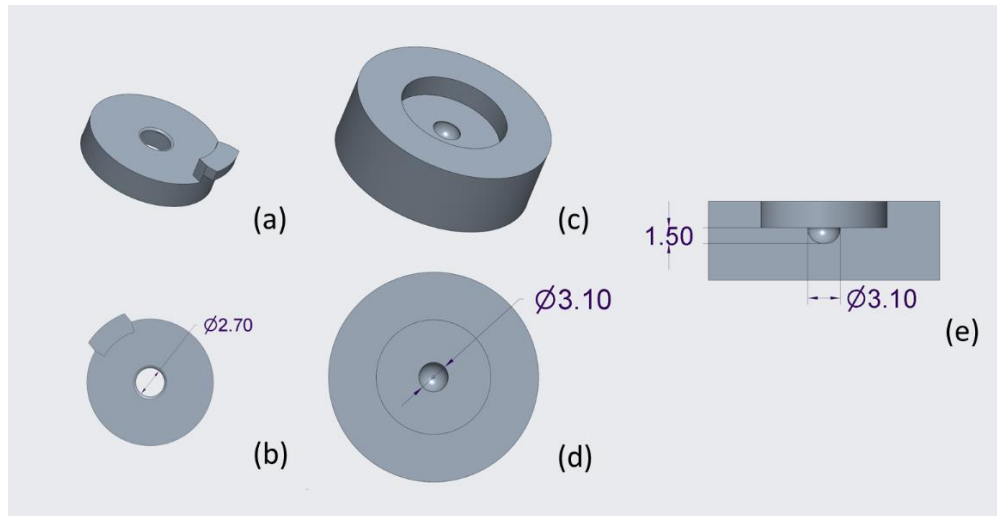


Figure 2. Design of the mouse retinal phantom. The dimensions stated were in mm. (a) and (b) show the designs and dimensions of the iris phantom. (c) and (d) show the design and dimensions of the anterior chamber. (e) shows a slice view of the anterior chamber design.

Optical Modeling

We modelled two anatomical aspects of the mouse retina: The blood vessels (arteries and veins) and the vitreous humor. To simulate the blood vessels, we used carbon fibers with diameter experimentally found to be $5\ \mu\text{m}$ (Figure 1(b)). To simulate vitreous humor and mimic its consistency, Systane brand lubricant eye drops were used to fill the inner portion of the model.

To determine the magnification factor of a mouse retina imaging system, our mouse retinal phantom was used to estimate the size of blood vessels. This task is challenging due to the combined effects of magnification introduced by both the endoscope and the mouse lens. The phantom model was imaged with an RGB camera at a focal depth simulating that used in live retinal imaging setups. ImageJ software was utilized to extract pixel length measurements of individual carbon fiber strands.

To calculate the magnification factor, a 1 mm marker with 0.1 mm increments was imaged, and the pixel measurements were recorded. The mouse eye phantom was then imaged using the same setup under two configurations: with the endoscope only and with the endoscope combined with the model lens. The measured pixel lengths of the carbon fibers under each configuration were converted to millimeters using the corresponding magnification factor. Figure 3 illustrates the relationship between the pixel lengths of the carbon fibers and their calculated lengths in millimeters for both configurations, yielding highly linear correlations with correlation coefficients of 0.9924 and 0.9913, respectively. For the phantom imaged with the endoscope only, the pixel-to-millimeter ratio was determined to be 452.44 pixels/mm, while for the setup with the endoscope and the model lens, the ratio was 544.28 pixels/mm. Minor variations in pixel measurements may be attributed to human error during manual measurements, as well as potential warping and slight shifts in fiber configuration between acquisition of images.

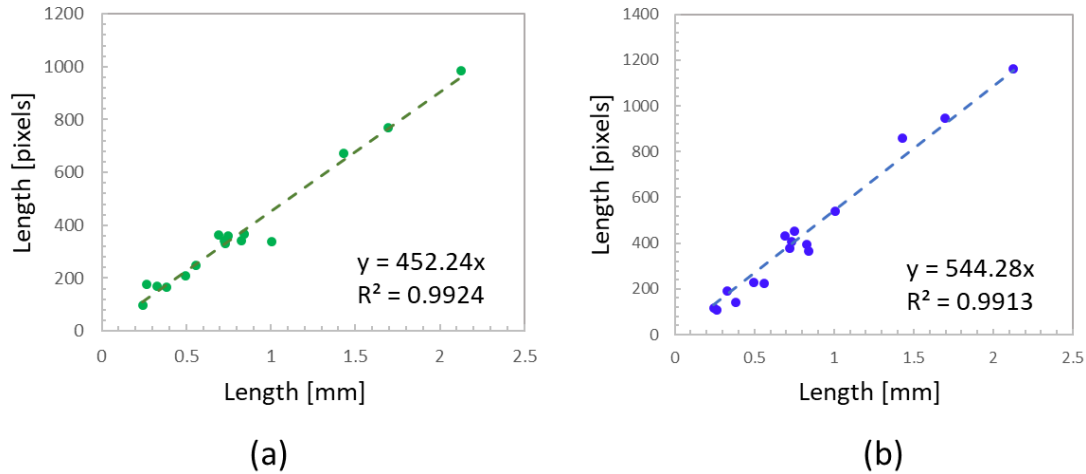


Figure 3. Plots of carbon fiber lengths in pixels versus lengths in millimeters for (a) the endoscope-only configuration, and (b) the endoscope with the mouse lens configuration.

Blood Vessel Modeling

We built a preliminary phantom using gelatin to simulate small blood vessels and validate the spectral ability of the HSI camera. Defibrinated sheep blood with 36% hematocrit (QuadFive, Montana, USA) was used to produce blood samples. We first oxygenated the blood by stirring it using a magnetic stirrer. 100% oxygenation rate was confirmed using a spectrophotometer.

Sodium dithionite solution was prepared by mixing 1 gram of sodium dithionite salt (Reagents, North Carolina, USA) into 40 mL of phosphate buffer saline (PBS) solution (Fisher Scientific, Massachusetts, USA) at room temperature and 7.4 pH. The solution was sparged with nitrogen gas beforehand to remove dissolved oxygen. We then diluted sodium dithionite-PBS solution into blood to produce concentrations of sodium dithionite at 0.5, 1.0, 1.4, 2.5, and 4.0 mg/mL of blood. The gelatin body was made using a combination of 10% gelatin (Type B, Fisher Chemical) to 90% deionized water. Using hematocrit tubes with inner diameters of 1.1 mm, we drew blood samples of different sodium dithionite concentrations. Figure 4(a) shows an example of a blood phantom. Figure 4(b) shows the image of the blood phantom taken at different wavelengths.

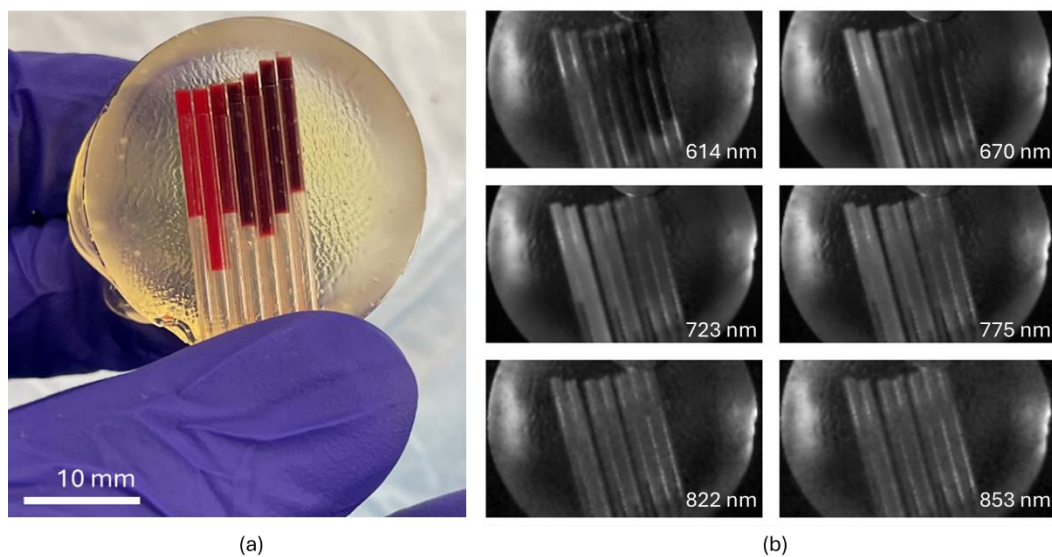


Figure 4. (a) RGB images of the phantom. (b) Hyperspectral image of the phantom taken at different wavelengths.

Image Acquisition

Figure 5 illustrates the imaging setup used to capture images of the mouse retinal phantom. A modified topical fundus imaging (TEFI) system was utilized for dual-camera imaging, integrating both hyperspectral (HSI) and RGB modalities. The system included a customized snapshot HSI camera, a high-resolution RGB camera, a 50:50 optical beam splitter, imaging endoscopes, and fixed focal length lenses. The HSI camera captured 15 spectral bands with an image resolution of 270×512 pixels within the 610–850 nm range [31]. The RGB camera, a scientific CMOS model (ToupTek C3CMOS series), captured images at resolutions up to 2048×3072 pixels. Both systems were mounted on a translation stage (ThorLabs, USA) itself positioned atop a rotational platform (ThorLabs, USA) (Figure 5). This configuration provided the system with four degrees of freedom (three rotational and one translational) for targeting various objects. A separate translating stage (ThorLabs, USA) allowed for vertical adjustment of the subject to bring the pupil into focus. Exposure times were set at 100 ms for the RGB camera and 150 ms for the HSI camera. A halogen light source with a spectral range extending into the near-infrared (NIR) provided illumination. The acquisition of gelatin phantoms was performed using a similar setup. The snapshot camera was connected to an Olympus surgical laparoscope with a 10 mm diameter tip placed 10 mm from the blood sample surface. Halogen light served as the illumination source for these experiments.

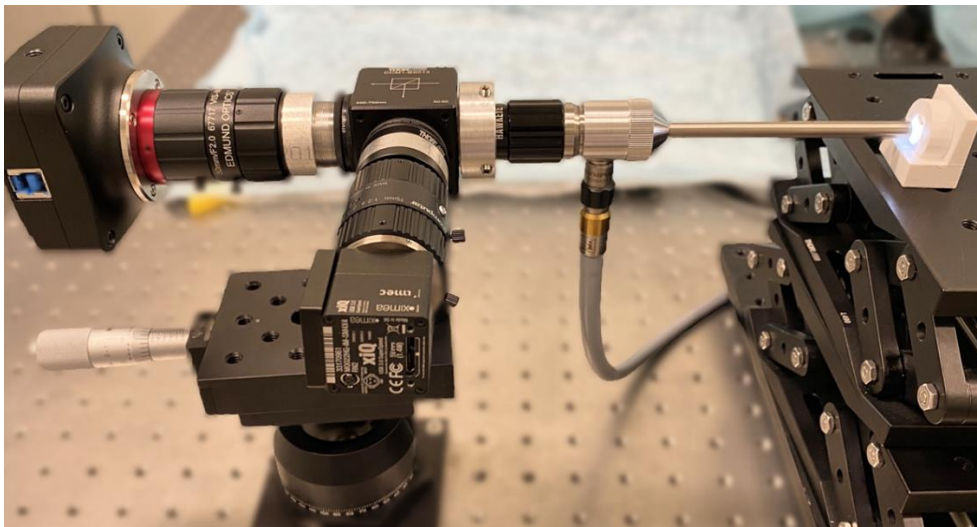


Figure 5. Imaging setup featuring dual-camera (HSI and RGB) integration with a surgical laparoscope positioned above the mouse retinal phantom. The system is mounted on adjustable translation and rotational platforms for precise alignment.

Image Analysis

Prior to imaging subjects, we acquired dark and white references by using a 95% reflective Spectralon target [1]. The raw image was normalized using white and dark reference. To analyze the retinal phantom images, we selected pixels belonging to the vessels and pixels belonging to the background, then compared their spectral differences.

To analyze the gelatin phantom, best-fit theoretical curves were used to produce oxygenation curves at 100% and 0%. All curves were normalized by their isosbestic value at 805 nm. If we assume that oxygenated and deoxygenated hemoglobin are the two primary chromophores, then the resulting spectra is simply the linear combination of the spectra of oxygenated and deoxygenated hemoglobin. If the theoretical reflectance of fully oxygenated blood is R_{oxy} , the reflectance of fully deoxygenated blood is R_{deoxy} , the reflectance of our sample is R_{sample} , then we estimated the oxygenation rate using the formula:

$$\text{SO}_2\% \text{ of sample} = \frac{R_{sample} - R_{deoxy}}{R_{oxy} - R_{deoxy}} \times 100\%$$

Since there are considerable differences in normalized reflectance between oxygenated and deoxygenated hemoglobin at 650 – 700 nm [32], we decided to calculate the samples' oxygenation rates by using the summed spectra from 650 – 700 nm.

3. RESULTS

Figure 6 shows the sample image taken using the TEFI beamsplitter system. The image shows that carbon fibers of diameter $5\ \mu\text{m}$ can be scanned using the system. There are some glares in the images, which are likely due to the light pattern of the imaging endoscopes.

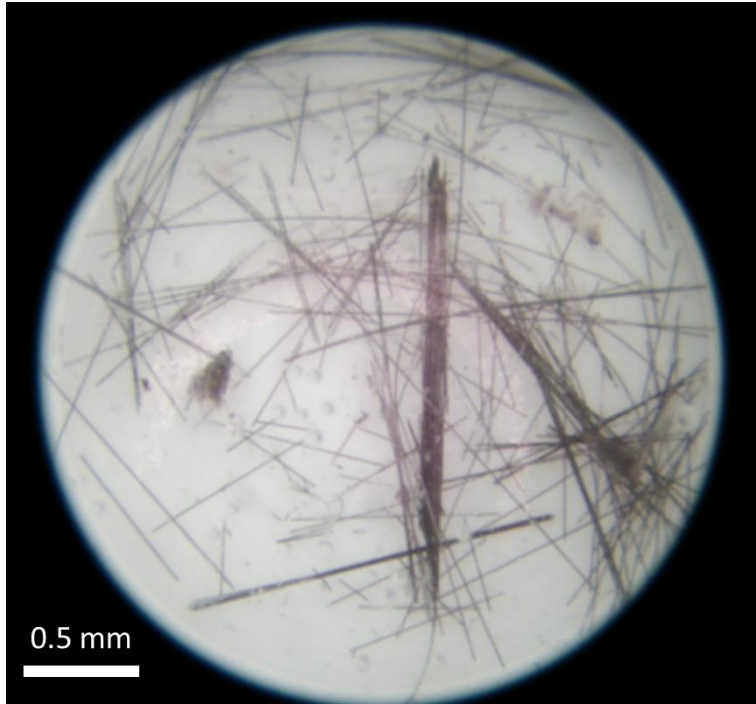


Figure 6. Mouse retina phantom model image with carbon fibers.

Figure 7 illustrates the relationship between sodium dithionite concentration in blood oxygenation tubes for blood vessel mapping and its effect on estimated oxygenation levels. In Figure 7(a), the isosbestic normalized reflectance values show a clear negative correlation with sodium dithionite concentrations, plateauing at approximately $2.4\ \text{mg/mL}$. Figure 7(b) presents the estimated hemoglobin oxygenation levels calculated from sample intensities at $660\ \text{nm}$, with a linear correlation coefficient of 0.9476 . Complete deoxygenation (0% oxygenation) is observed at approximately $2.19\ \text{mg/mL}$.

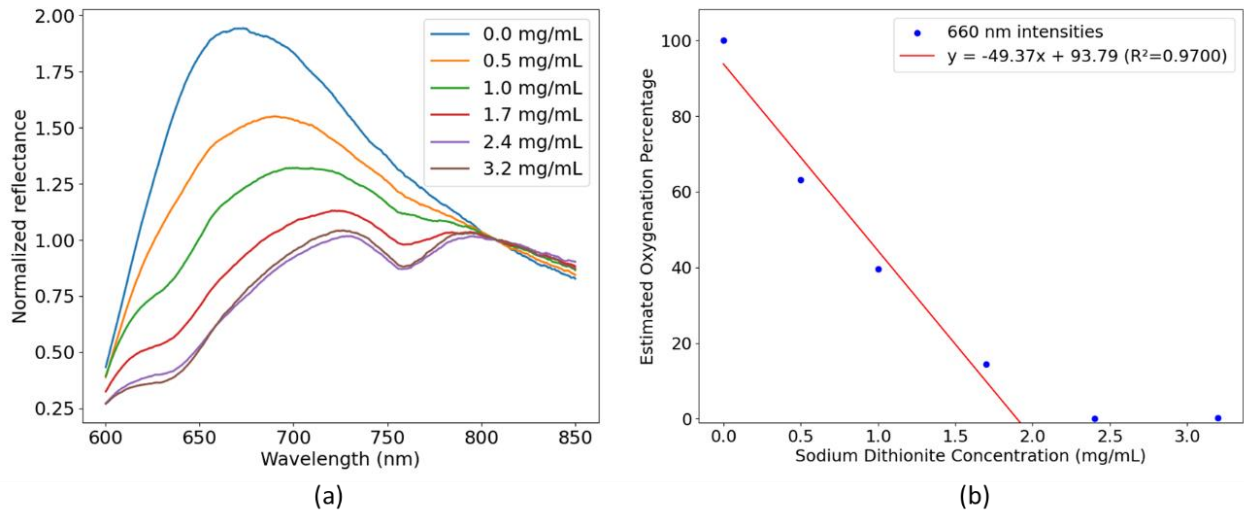


Figure 7. (a) Isosbestic normalized reflectance values of blood with increasing concentrations of sodium dithionite across the 600-850 nm RNIR range. (b) Estimated oxygenation percentages of hemoglobin were calculated using intensity values at 660 nm at increasing concentrations of sodium dithionite.

Figure 8 shows the results of the blood oxygen tubes with samples at different oxygen levels. In Figure 8(a), the oxygen concentration mapping results are displayed, showing the spatial distribution of oxygen levels as captured by the snapshot camera. The oxygen concentration mapping correctly localized oxygen levels within each capillary tube. Despite the small size of each tube (~ 1mm in diameter, comparable to human arteries), the optical configurations of the snapshot camera and endoscope could still separate the tubes visually, showing good spatial resolution. Figure 8(b) presents the expected oxygenation rates for different tubes, which were calculated using sodium dithionite concentrations. Figure 8(c) depicts the differences in errors between the measured and expected oxygenation rates. An average error of 7.5% in the oxygenation rate measurements was observed. The oxygenation rates were most accurately estimated at higher values, specifically within the 60% to 100% range. However, the accuracy was lower at lower oxygenation rates, specifically below 20%. Looking at Figure 8(c), we also noticed that the errors were localized toward the edges of the blood tubes, most likely due to refraction and scattering at the edge of the tubes.

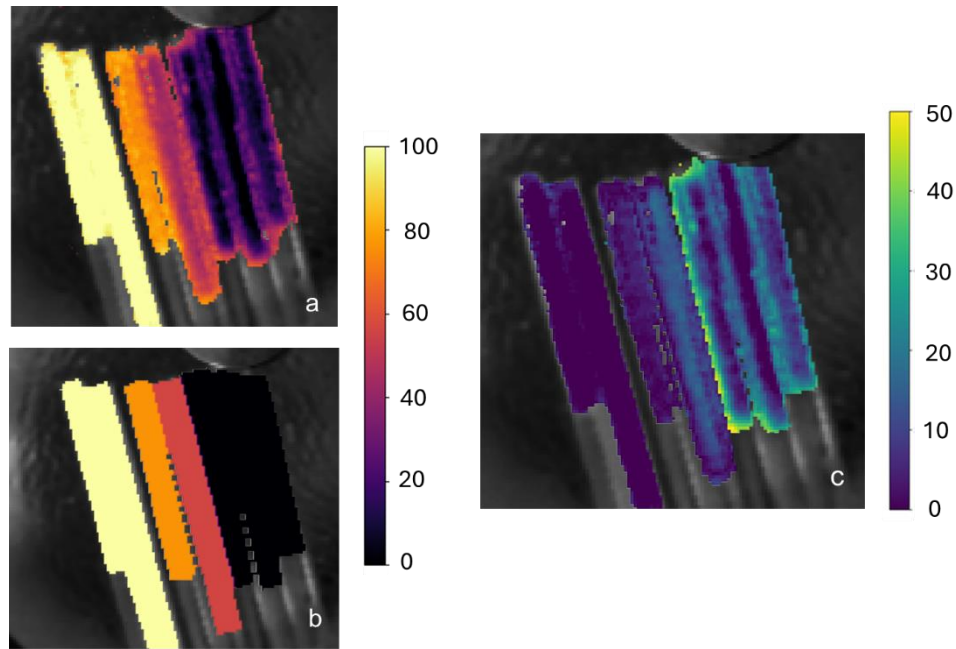


Figure 8. (a) Estimated oxygenation rate from oxygenation mapping. (b) Expected oxygenation rate calculated using concentration of sodium dithionite. (c) Error differences between estimated and expected oxygenation rates. Units of color bar is in percentage.

4. DISCUSSION AND CONCLUSION

In this study, we designed a mouse retina model for hyperspectral imaging. We presented the following new works: First, a retinal phantom was designed and developed to mimic the optical characteristics of mouse retina. The phantom body was 3D printed, and the optical components were procured at low cost from off-the-shelf components. Second, a gelatin phantom was developed that mimics the spectral characteristics of veins and arteries. Blood samples were produced using sodium dithionite to generate predictable oxygen saturation levels. Our design included more accurate anatomical modeling, selecting an optical medium that mimics vitreous humor, and a validation study using a gelatin phantom. The development of such phantoms can test the spatial and spectral abilities of HSI cameras and can be translated into animal studies. While we do not have a phantom that can approximate both spatial and spectral details at the same time, we believe that it is a possible endeavor and worthy of investigation in the future.

Our method involved 3D printing the lens holder to ensure precise alignment and stability during imaging, followed by validation of the phantom's optical properties through imaging tests. We produced a pixel-to-mm ratio of imaging configuration simulating focal depth and magnification of live animal retinal imaging systems. Manual measurement of pixel lengths in carbon fibers using ImageJ software may introduce human error; however, the strong correlation coefficient in the linear trend data in Figure 3 indicates the reliability of the measurements. This approach is offered as a simple and effective noninvasive calculation of retinal blood vessel diameters. We hope to demonstrate enhanced image clarity and consistency compared to traditional models. This phantom serves as a versatile tool for standardizing imaging protocols, developing new imaging technologies, and reducing reliance on live animal models. By providing a reproducible, customizable platform, this work advances retinal research, with potential applications in surgical training, educational settings, and preclinical testing of retinal therapies.

ACKNOWLEDGMENTS

Research reported in this publication was supported in part by the National Cancer Institute of the National Institutes of Health under Award Number R01CA288379 and R01CA204254, by the Cancer Prevention and Research Institute of

Texas (CPRIT) under Award Number RP240289 and RP240542, and by the Eugene McDermott Graduate Fellowship (EMGF) 202009 at the University of Texas at Dallas. The content is solely the responsibility of the authors and does not necessarily represent the official views of the National Institutes of Health.

REFERENCES

- [1] G. Lu and B. Fei, "Medical hyperspectral imaging: a review," (in eng), *J Biomed Opt*, vol. 19, no. 1, p. 10901, Jan 2014, doi: 10.1117/1.Jbo.19.1.010901.
- [2] M. H. Tran and B. Fei, "Compact and ultracompact spectral imagers: technology and applications in biomedical imaging," *Journal of Biomedical Optics*, vol. 28, no. 4, p. 040901, 4/1 2023, doi: 10.1117/1.JBO.28.4.040901.
- [3] X. Hadoux *et al.*, "Non-invasive in vivo hyperspectral imaging of the retina for potential biomarker use in Alzheimer's disease," *Nature Communications*, vol. 10, no. 1, p. 4227, 2019/09/17 2019, doi: 10.1038/s41467-019-12242-1.
- [4] B. Fei *et al.*, "Label-free reflectance hyperspectral imaging for tumor margin assessment: a pilot study on surgical specimens of cancer patients," *Journal of Biomedical Optics*, vol. 22, no. 8, p. 086009, 8/1 2017, doi: 10.1117/1.JBO.22.8.086009.
- [5] N. Lee *et al.*, "In vivo snapshot hyperspectral image analysis of age-related macular degeneration," in *2010 Annual International Conference of the IEEE Engineering in Medicine and Biology*, 31 Aug.-4 Sept. 2010 2010, pp. 5363-5366, doi: 10.1109/IEMBS.2010.5626463.
- [6] M. S. Chin *et al.*, "Hyperspectral Imaging for Burn Depth Assessment in an Animal Model," *Plastic and Reconstructive Surgery – Global Open*, vol. 3, no. 12, 2015, doi: 10.1097/GOX.0000000000000558.
- [7] A. Schmidt *et al.*, "Hyperspectral Imaging of Wounds Reveals Augmented Tissue Oxygenation Following Cold Physical Plasma Treatment in Vivo," *IEEE Transactions on Radiation and Plasma Medical Sciences*, vol. 5, no. 3, pp. 412-419, 2021, doi: 10.1109/TRPMS.2020.3009913.
- [8] D. Sakota *et al.*, "Hyperspectral imaging of vascular anastomosis associated with blood flow and hemoglobin concentration," in *2015 37th Annual International Conference of the IEEE Engineering in Medicine and Biology Society (EMBC)*, 25-29 Aug. 2015 2015, pp. 4246-4249, doi: 10.1109/EMBC.2015.7319332.
- [9] D. J. Mordant *et al.*, "Oxygen saturation measurements of the retinal vasculature in treated asymmetrical primary open-angle glaucoma using hyperspectral imaging," *Eye*, vol. 28, no. 10, pp. 1190-1200, 2014/10/01 2014, doi: 10.1038/eye.2014.169.
- [10] H. Akbari *et al.*, "Blood vessel detection and artery-vein differentiation using hyperspectral imaging," in *2009 Annual International Conference of the IEEE Engineering in Medicine and Biology Society*, 3-6 Sept. 2009 2009, pp. 1461-1464, doi: 10.1109/IEMBS.2009.5332920.
- [11] M. H. Fouad *et al.*, "Delineation of the Arm Blood Vessels Utilizing Hyperspectral Imaging to Assist with Phlebotomy for Exploiting the Cutaneous Tissue Oxygen Concentration," *Photodiagnosis and Photodynamic Therapy*, vol. 33, p. 102190, 2021/03/01/ 2021, doi: <https://doi.org/10.1016/j.pdpdt.2021.102190>.
- [12] S. Lemmens *et al.*, "Hyperspectral Imaging and the Retina: Worth the Wave?," *Translational Vision Science & Technology*, vol. 9, no. 9, pp. 9-9, 2020, doi: 10.1167/tvst.9.9.9.
- [13] A. R. Harvey and D. W. Fletcher-Holmes, "Birefringent Fourier-transform imaging spectrometer," *Optics Express*, vol. 12, no. 22, pp. 5368-5374, 2004.
- [14] Q. Li *et al.*, "New microscopic pushbroom hyperspectral imaging system for application in diabetic retinopathy research," *Journal of Biomedical Optics*, vol. 12, no. 6, p. 064011, 11/1 2007, doi: 10.1117/1.2821210.
- [15] K. Rose *et al.*, "Retinal perfusion changes in radiation retinopathy," *Acta Ophthalmologica*, vol. 96, no. 6, pp. e727-e731, 2018, doi: <https://doi.org/10.1111/aos.13797>.
- [16] S. S. More *et al.*, "Early detection of amyloidopathy in Alzheimer's mice by hyperspectral endoscopy," *Investigative ophthalmology & visual science*, vol. 57, no. 7, pp. 3231-3238, 2016.
- [17] H.-Y. Yao *et al.*, "Hyperspectral Ophthalmoscope Images for the Diagnosis of Diabetic Retinopathy Stage," *Journal of Clinical Medicine*, vol. 9, no. 6, p. 1613, 2020.
- [18] J. Kaluzny *et al.*, "Bayer filter snapshot hyperspectral fundus camera for human retinal imaging," *Current eye research*, vol. 42, no. 4, pp. 629-635, 2017.
- [19] G. Lu *et al.*, "Estimation of tissue optical parameters with hyperspectral imaging and spectral unmixing," in *Medical Imaging 2015: Biomedical Applications in Molecular, Structural, and Functional Imaging*, 2015, vol. 9417: International Society for Optics and Photonics, p. 94170Q.

- [20] A. S. Luthman *et al.*, "Bimodal reflectance and fluorescence multispectral endoscopy based on spectrally resolving detector arrays," *Journal of biomedical optics*, vol. 24, no. 3, p. 031009, 2018.
- [21] P. Liu *et al.*, "Multiview hyperspectral topography of tissue structural and functional characteristics," *Journal of biomedical optics*, vol. 21, no. 1, p. 016012, 2016.
- [22] N. Liu *et al.*, "Integrated photoacoustic and hyperspectral dual-modality microscopy for co-imaging of melanoma and cutaneous squamous cell carcinoma in vivo," (in eng), *J Biophotonics*, vol. 13, no. 8, p. e202000105, Aug 2020, doi: 10.1002/jbio.202000105.
- [23] P. Ghassemi *et al.*, "Rapid prototyping of biomimetic vascular phantoms for hyperspectral reflectance imaging," *Journal of Biomedical Optics*, vol. 20, no. 12, p. 121312, 2015.
- [24] M. Paques *et al.*, "Panretinal, High-Resolution Color Photography of the Mouse Fundus," *Investigative Ophthalmology & Visual Science*, vol. 48, no. 6, pp. 2769-2774, 2007, doi: 10.1167/iovs.06-1099.
- [25] Z. Hosseinaee *et al.*, "In-vivo functional and structural retinal imaging using multiwavelength photoacoustic remote sensing microscopy," (in eng), *Sci Rep*, vol. 12, no. 1, p. 4562, Mar 16 2022, doi: 10.1038/s41598-022-08508-2.
- [26] S. Remtulla and P. E. Hallett, "A schematic eye for the mouse, and comparisons with the rat," (in eng), *Vision Res*, vol. 25, no. 1, pp. 21-31, 1985, doi: 10.1016/0042-6989(85)90076-8.
- [27] M. N. Polyanskiy, "Refractiveindex.info database of optical constants," *Scientific Data*, vol. 11, no. 1, p. 94, 2024/01/18 2024, doi: 10.1038/s41597-023-02898-2.
- [28] C. Cheng *et al.*, "Age-related changes in eye lens biomechanics, morphology, refractive index and transparency," *Aging (Albany NY)*, vol. 11, pp. 12497 - 12531, 2019. [Online]. Available: <https://pmc.ncbi.nlm.nih.gov/articles/PMC6949082/pdf/aging-11-102584.pdf>.
- [29] J. M. Skeie *et al.*, "Evisceration of Mouse Vitreous and Retina for Proteomic Analyses," *JoVE*, no. 50, p. e2795, 2011/04/03/ 2011, doi: doi:10.3791/2795.
- [30] J. M. Skeie and V. B. Mahajan, "Proteomic interactions in the mouse vitreous-retina complex," (in eng), *PLoS One*, vol. 8, no. 11, p. e82140, 2013, doi: 10.1371/journal.pone.0082140.
- [31] S. Lemmens *et al.*, "Combination of snapshot hyperspectral retinal imaging and optical coherence tomography to identify Alzheimer's disease patients," (in eng), *Alzheimers Res Ther*, vol. 12, no. 1, p. 144, Nov 10 2020, doi: 10.1186/s13195-020-00715-1.
- [32] S. Prahl. Optical absorption of hemoglobin [Online] Available: <http://omlc.ogi.edu/spectra/hemoglobin>